Cylinder head temperature determination using high-speed phosphor thermometry in a fired internal combustion engine

**N. Fuhrmann · C. Litterscheid · C.-P. Ding ·
J. Brübach · B. Albert · A. Dreizler**

Abstract This paper documents the application of high-speed phosphor thermometry to measure cylinder head temperatures under fired engine conditions. The thermographic phosphor $Gd_3Ga_5O_{12}$:Cr,Ce was synthesized with a special composition to meet the requirements of the measurement technique and the device under test. Calibration measurements are given in the first section, providing the temperature lifetime characteristic and temporal standard deviations in order to quantify single-shot precision. Accuracy was investigated for laser-induced heating. Measurements inside an optically accessible combustion engine are presented in the second section. Measurement locations at the cylinder head were determined, as well as temperature evolutions for variations in spark timing and air–fuel ratio.

N. Fuhrmann (✉) · C.-P. Ding · J. Brübach · A. Dreizler
Fachgebiet Reaktive Strömungen und Messtechnik (RSM),
Center of Smart Interfaces (CSI), Technische Universität
Darmstadt, Petersenstraße 32, 64287 Darmstadt, Germany
e-mail: fuhrmann@csi.tu-darmstadt.de

C.-P. Ding
e-mail: ding@csi.tu-darmstadt.de

J. Brübach
e-mail: bruebach@ekt.tu-darmstadt.de

A. Dreizler
e-mail: dreizler@csi.tu-darmstadt.de

C. Litterscheid · B. Albert
Eduard-Zintl-Institut für Anorganische und Physikalische
Chemie, Technische Universität Darmstadt, Petersenstraße 18,
64287 Darmstadt, Germany
e-mail: litterscheid@ac.chemie.tu-darmstadt.de

B. Albert
e-mail: albert@ac.chemie.tu-darmstadt.de

1 Introduction

Temperature distributions of in-cylinder surfaces play a crucial role in the development of internal combustion engines (ICE). In particular, in the context of downsizing, temperatures and temperature gradients along the surface of engine components during operation are increasing in importance. Wall temperatures are needed as boundary conditions in computational fluid dynamics (CFD) to predict, i.e., heat losses and gas-phase temperatures accurately [1]. In the past, surface temperature measurements inside ICEs were mainly taken using surface thermocouples and thermographic phosphors. The use of thermocouples is widely established and regularly [2–4]. However, it is limited to zero-dimensional measurements, and the complexity of the installation of thermocouples in ICEs is significant. Thermographic phosphors are usually used to determine surface temperatures zero- or two-dimensionally [5–7]. Phosphor thermometry relies on the temperature-dependent change in emission properties of ceramic materials, doped with rare earth or transition metals. To perform surface temperature measurements, the thermographic phosphor material has to be coated on the device under test. Upon laser excitation, either the ratio of two spectrally separated signals (intensity ratio approach) [8–11] or the temporally resolved (lifetime approach) luminescence [12–15] can be detected with an appropriate device and subsequently evaluated for thermometry purposes. A recent investigation revealed the high potential for systematic errors in the intensity ratio approach [16]. Therefore, the determination of the temperature-dependent

luminescence lifetime was chosen for the application in this work.

The application of phosphor thermometry in ICEs was first demonstrated by Armfield et al. [17] in a study that comprised zero-dimensional temperature determinations of cylinder head and intake valves in an optically accessible ICE using the lifetime approach. Further studies included recordings of two-dimensional temperature fields using error-prone spectrally integrated measurements [18] as well as point-wise determined piston and cylinder wall temperatures (lifetime approach) [19, 20]. The lifetime approach was extended to two-dimensions by the use of a CCD framing camera [18] or modern CMOS high-speed cameras [21, 22]. All of the aforementioned studies were carried out using conventional laser systems with repetition rates in the order of 10 Hz. This implies that single-shot measurements can only be performed in subsequent cycles that are not statistically correlated. To overcome this limitation, a high-speed laser system was applied and characterized to determine temperatures point-wise in a motored engine (no combustion) [23]. This investigation demonstrated that temperature information can be obtained with one measurement per crank angle at 1,000 rpm using high-speed phosphor thermometry.

This paper investigates the use of this technique in a fired ICE (with combustion), whereas previous studies based on the high-speed phosphor thermometry were restricted to motored engine operation only. For this purpose, the thermographic phosphor $Gd_3Ga_5O_{12}$:Cr,Ce is synthesized to match the temperature range specific for fired engine operation. Prior to its engine application, the co-doped phosphor was characterized in terms of precision and accuracy. Application-oriented synthesis of well-defined thermographic phosphors has proven to result in broad applicability of this method for temperature measurements [24, 25]. The in-cylinder measurements performed incorporate zero-dimensional surface thermometry at different positions at the cylinder head and a variation in spark timing (ST) and air–fuel ratio.

2 Experimental setup

This Section documents experimental setups for characterization, calibration, and in-cylinder measurements. Instrumentation was the same in both experimental arrangements.

2.1 X-ray diffraction

X-ray powder diffraction data of the synthesized $Gd_3Ga_5O_{12}$:Cr,Ce were collected at room temperature by a powder diffractometer (STOE Stadi P, linear PSD) with Cu radiation (Ge monochromator, $\lambda = 1.540598$ Å, flat plate sample holder, transmission geometry). For Rietveld refinement, the published structure [26] was chosen as a starting model and the TOPAS suite of programs [27] was used. All atoms were refined freely using positional and isotropic displacement parameters.

2.2 Calibration measurements

Luminescence was excited by a frequency quadrupled, diode-laser-pumped Nd:YAG laser (Edgewave CX16II-E 80 W). Single-shot laser energies were adjusted by the combination of a half-wave plate and a glan polarizer. The power of the laser beam was monitored by a power meter (Gentec UP19K-150W-H5-D0). The calibration measurements were performed inside a tube furnace (Carbolite, CTF 12/100/00). For calibration purposes, the laser beam has been directed onto a phosphor-coated stainless steel substrate that was mounted to a type N thermocouple inside the furnace.

The detection of the time-resolved phosphorescence decay was accomplished by a photomultiplier tube (Hamamatsu, H6780-20), employing a Carl Zeiss T*85 mm photo lens, a planar convex lens, and an interference filter ($\lambda_c = 700$ nm, FWHM = 40 nm). The spatial resolution of the system was approximately 0.8 mm^2. The photomultiplier current was read out by an oscilloscope (Tektronix TDS 5032B) at an input resistance of 512 Ω. The laser optical setup is shown in Fig. 1. The acquisition of the temperature lifetime characteristic was performed in the following order: First, the furnace was heated until the reference thermocouple indicated the maximum desired temperature. Subsequently, the heating was switched off and data were acquired during cooling. The average cooling rate was 0.03 Ks^{-1}, which corresponds to an average temperature change of 6 mK during the acquisition of 500 single-
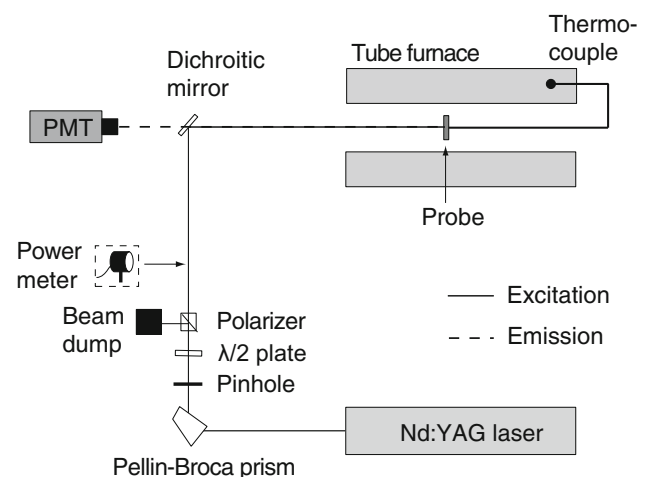

Fig. 1 Laser optical setup for calibration measurements

shots at 1 kHz. The experimental setup for the detection of the luminescence spectra was basically the same as the one shown in Fig. 1. In order to resolve the luminescence intensity spectrally, the photomultiplier tube has been replaced by a fiber-coupled spectrometer (Stellar Net STE-EPP2000-C, grating 600 lines/mm, slit width 50 μm, maximum resolution 1.5 nm). The transfer function of the spectrometer was corrected by a spectrally calibrated light source (Ulbricht sphere, Gigahertz-Optik UMBB-300).

2.3 Optically accessible internal combustion engine

The device under test was the optically accessible four-stroke ICE at Technische Universität Darmstadt. The engine featured a pent-roof cylinder head and was equipped with a quartz glass ring and piston insert to guarantee optical access. The geometry and operational parameters of the ICE are listed in Table 1. The engine was operated in work-rest mode with 400 fired and 800 motored cycles.

The laser optical setup is shown in Fig. 2. Excitation and emission are both reflected by the broadband mirror above the crank case and transmitted through the flat piston window. A dichroic mirror ($R_{266nm} > 97$ %, $T_{700-750nm} > 85$ %) separated excitation and emission. The entire cylinder head was coated with a dispersion of SP-115 (VHT Paints, AZ, USA) and the phosphor $Gd_3Ga_5O_{12}$:Cr,Ce using an airbrush so that measurement locations could be chosen individually. The thickness of the phosphor coating could not be determined accurately due to the complex
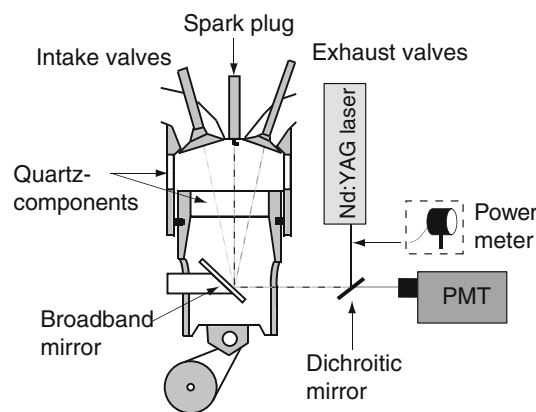

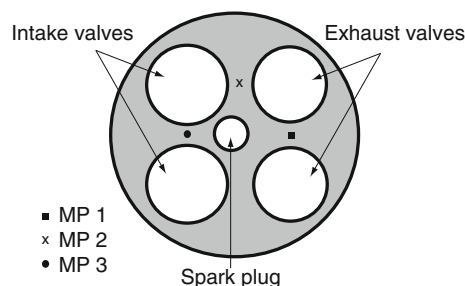Fig. 2 Laser optical setup for in-cylinder measurements

Fig. 3 Location of measurement points at the cylinder head

geometry and topology of the cylinder head surface. However, reference measurements under controlled conditions showed a coating thickness of about 20 μm using identical settings for the airbrush gun, the phosphor binder mixture, and the coating timing. According to the measurements conducted by Knappe et al. [20], thicknesses above 30 μm result in systematic errors of several K. The results shown in this study are therefore believed to be free of major systematic errors concerning this heat conductivity issue discussed in the literature [20, 28]. The different measurement points (MP) are shown in Fig. 3. The reference spot, which was also subject to changes in air–fuel ratio and spark timing, was located between the exhaust valves (MP1). For spatial variations, locations in between exhaust and intake valves (MP2) as well as in between the intake valves (MP3) were selected.

3 Data evaluation

3.1 Lifetime determination

To evaluate the decay curves on a single-shot basis, the linear regression of the sum (LRS) was applied to determine the decay time τ [29]. The waveform is modeled as mono-exponential decay of the form

Table 1 Engine parameters

Displacement volume	499 cm^3
Stroke	86 mm
Bore	86 mm
Compression ratio	8.5:1
Temperature of cooling fluids	333 K
Temperature of intake air	313 K
Intake valves	
Open at	326 CAD
Close at	−126 CAD
Lift	10 mm
Exhaust valves	
Open at	106 CAD
Close at	−344 CAD
Lift	10 mm
Speed	1,000 rpm
Injection	port-fuel, iso-octane
Starting at	−120 CAD
Duration	6.7 ms
Air/fuel ratio	1.2
Mean effective pressure	5.36 bar

$$I(t) = I_0 \, e^{-\frac{t}{\tau}} + b, \tag{1}$$

where t denotes the time, I_0 is the intensity at $t = 0$, and b is an offset that is usually determined by averaging signal prior to laser excitation (Sect. 3.2). LRS uses the fact that the integral of Eq. 1 with known parameter b equals

$$\int_0^t I(t)\mathrm{d}t = \int_0^t (I_o \exp^{-\frac{t}{\tau}})\mathrm{d}t = \tau I_0 - \tau I(t). \tag{2}$$

Rearranging Eq. 2 leads to

$$I(t) = I_0 - \frac{1}{\tau}\int_0^t I(t)\mathrm{d}t, \tag{3}$$

showing that $I(t)$ can be written as a function of its own integral. Hence, conventional least-squares fitting or an analytic solution by approximating the integral as a sum can then be applied to determine τ [29]. LRS has precision levels comparable to those achieved when using a Levenberg–Marquardt algorithm but has computational time benefits to a factor of 20 [30].

To determine the temporal boundaries where fitting is performed, an iteratively adapted fitting window was applied [31]. This procedure defines the start (t_1) and the end (t_2) of the fitting window in dependence of τ:

$$t_1 = c_1\tau, \tag{4}$$

$$t_2 = c_2\tau, \tag{5}$$

where c_1 and c_2 are two constants that have to be set individually for each thermographic phosphor material. According to previous publications, the constants were $c_1 = 0.5$ and $c_2 = 3.5$ for the phosphor used in this study [32, 22].

3.2 Offset determination

As stated above, the time-independent offset b can be determined by averaging signal for $t < t_0$. However, during combustion, phosphorescence and flame luminosity interfere. The offset b in Eq. 1 then becomes time-dependent. To accomplish fitting in an accurate way, $b(t)$ needs to be determined. Generally, this can be accomplished in two ways:

1. Determination of $b(t)$ by phase averaging signals with flame luminosity but without laser excitation
2. In-situ extraction of $b(t)$ by isolating flame luminosity from phosphorescence on a single-shot basis.

Since cyclic fluctuations were significant, phase averaging of background signal using the first method and subsequent subtraction from single-shot phosphorescence signals of corresponding crank angles led to high systematic errors.

The second strategy resulted in fewer error-prone results and is therefore the method of choice here. Accordingly, this approach is discussed and explained in more detail.

Single-shots where the decaying waveform and flame luminosity interfered were identified by either higher mean signal values or increased standard deviations of the single-shot signal intensity for $t < t_0$. During engine measurements, the temporal discretization was set to 0.8 μ s and the number of data points per decay curve was 500. This resulted in a total observation time for each measurement of 2.4 crank angle degrees (CAD) at an engine speed of 1000 rpm. Flame luminosity was assumed to result in a constant intensity gradient within this relatively short temporal window. Hence, the signal for $t < t_0$ was approximated by a linear regression and extrapolated for $t > t_0$. Subsequently, $b(t)$ was subtracted from $I(t)$ and the lifetime determination was performed. The entire procedure is illustrated in Fig. 4 for the example of a single-shot at 6 CAD.
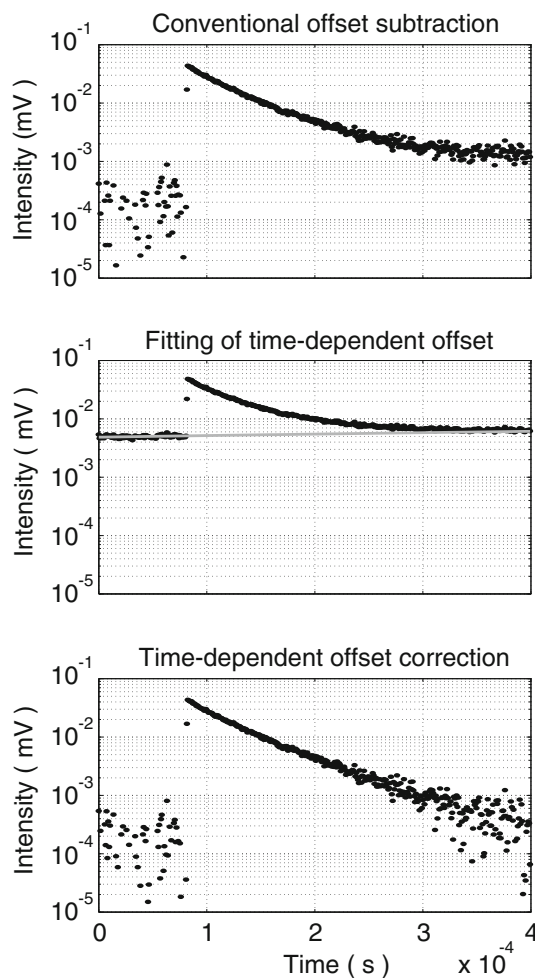

Fig. 4 Offset correction for a phosphorescence decay curve interfering with flame luminescence: Conventional offset subtraction (*top*), uncorrected signal and linear regression of the offset (*middle*) and subsequently performed correction (*bottom*)
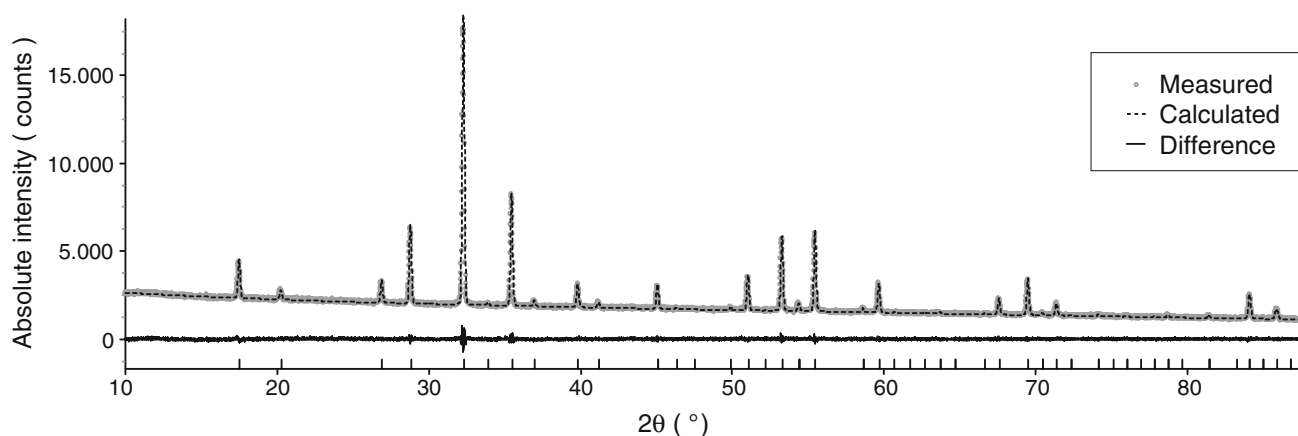
Fig. 5 Measured and calculated powder pattern and difference curve for $Gd_3Ga_5O_{12}$:Cr,Ce. *Vertical dashes* indicate the positions of the reflections of $Gd_3Ga_5O_{12}$:Cr,Ce

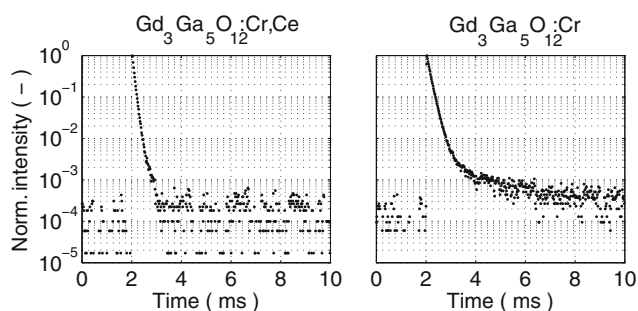**Fig. 6** Effect of reduced afterglow by co-doping $Gd_3Ga_5O_{12}$:Cr with Ce at room temperature

4 Phosphor Thermometry

Previous studies identified $Gd_3Ga_5O_{12}$:Cr as an appropriate candidate for lifetime-based phosphor thermometry in ICEs [32, 22]. The temperature lifetime characteristics of this material are such that decay times are fast enough to perform measurements at a repetition rate of up to 1 kHz at room temperature. However, when applying high-speed phosphor thermometry, it is vitally important for the luminescence to completely decay in between two laser shots to avoid interactions between subsequent measurements. Since $Gd_3Ga_5O_{12}$:Cr has a significant afterglow, the commercially available powder (Phosphor Technology Ltd.) is not suitable for this application. However, according to Blasse and co-workers [33], this afterglow can be reduced by co-doping the material with a small amount of Ce. Therefore, the following Sections document the synthesis and characterization of custom-made $Gd_3Ga_5O_{12}$:Cr,Ce.

4.1 Synthesis of $Gd_3Ga_5O_{12}$:Cr,Ce

For the synthesis of chromium-doped (2 mol%), cerium-co-doped (0.034 mol%) gadolinium gallium garnet ($Gd_3Ga_5O_{12}$:Cr,Ce), which crystallizes in the cubic crystal system (space group $Ia\,\bar{3}d$), Gd_2O_3 (Chempur, 99.99 %), $Cr(NO_3)_3 \cdot 9H_2O$ (Sigma-Aldrich, 99 %) and $(NH_4)_2Ce(NO_3)_6$ (Merck, 99 %) were dissolved in hot, diluted nitric acid (HNO_3) under magnetic stirring. A stoichiometric amount of fine-powdered Ga_2O_3 (Chempur, 99.99 %) was suspended in this solution. After two hours of stirring continuously, an NH_4OH solution was slowly added to increase the pH value of the suspension to 8, followed by stirring for a further hour. The obtained precipitate was filtered and then dried in air overnight at 378 K. Subsequently, the powder was ball-milled and finally fired in air at 1673 K for 6 hours.

In order to verify the successful synthesis of $Gd_3Ga_5O_{12}$:Cr,Ce in the form of pure crystalline powder, X-ray diffraction was performed. Calculated data were obtained by employing Rietveld refinements [34]. The results are shown in Fig. 5. The sample scattered very well and could easily be indexed. There were no additional or missing reflections that would indicate the choice of a different unit cell or the presence of unknown byproducts. For more details see supplemental material.

4.2 Characterization of $Gd_3Ga_5O_{12}$:Cr,Ce

The effect of co-doping $Gd_3Ga_5O_{12}$:Cr with Ce is shown in Fig. 6. The Figure compares at room temperature two single-shot decay waveforms to the commercially available powder and the one synthesized in this work. The long afterglow on the right-hand side of Fig. 6 vanishes due to the co-doping of $Gd_3Ga_5O_{12}$:Cr with Ce (left hand side of Fig. 6).

Figure 7 presents the emission spectrum of $Gd_3Ga_5O_{12}$:Cr,Ce upon laser excitation at 266 nm. The spectrum corresponds well with previous studies [32, 35], revealing its maximum at 730 nm and a broadband
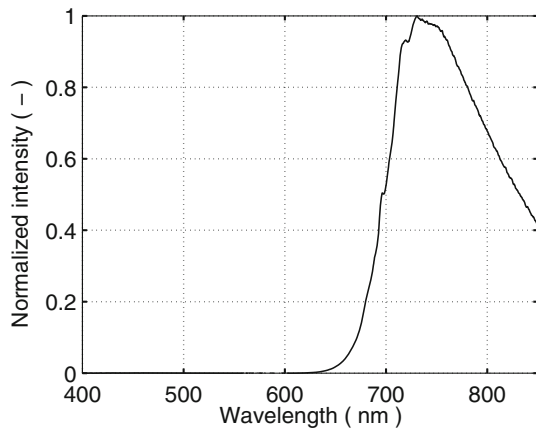
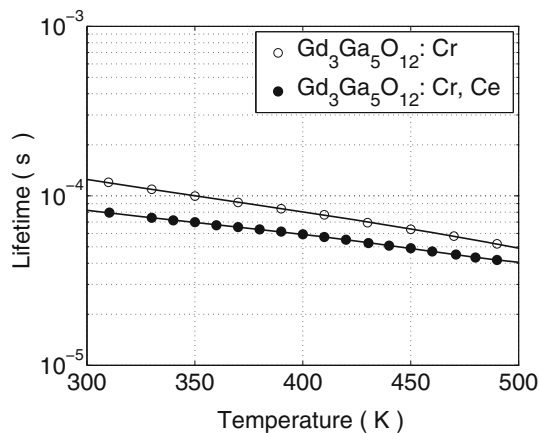**Fig. 7** Emission spectra of $Gd_3Ga_5O_{12}$:Cr,Ce upon UV laser excitation

Fig. 9 Relative temporal standard deviations of Gd3Ga5O12:Cr and Gd3Ga5O12:Cr,Ce.

identified to be higher than the one from the commercially available powder (unknown Cr concentration).

Figure 9 presents the relative temporal standard deviations that have been computed using

$$\frac{1}{\overline{T}}\sqrt{\frac{1}{N-1}\sum_{i=1}^{N_i}\left(T_i - \overline{T}\right)^2},\qquad(6)$$

with $\overline{T} = \frac{1}{N}\sum_{i=1}^{N} T_i$, are plotted versus temperature to indicate temperature-dependent single-shot precision. Up until 400 K, both materials investigated reveal very similar precisions in the order of 0.5 to 0.7 %. For higher temperatures, the precision of the custom-made material is superior by almost a factor of 2 compared to the commercially available phosphor. However, this difference could not explicitly be traced back to the material and could be due to the settings of the detection system.

Laser-induced heating has to be investigated when applying high-speed phosphor thermometry in order to avoid systematic errors [23]. Therefore, an energy scan was performed at MP1 while the engine was at standstill, with cooling fluid temperatures of 333 K. The results are shown in Fig. 10. Note that the temperatures presented in this Figure were computed using the temperature lifetime characteristic in Fig. 8, which was acquired at a single-shot laser energy of 0.13 mJ. For each setting of laser pulse energy, mean values and standard deviations (according to Eq. 6) are shown. Additionally, a quadratic polynomial has been added to guide the eyes. It can be seen that increasing single-shot energies leads to an increase in apparent temperatures. In order to select the optimum energy for the subsequent measurements, the least heating is desired at an optimum signal-to-noise ratio (SNR), which means that the signal is slightly below the saturation limit of the photomultiplier tube. According to this, a single-shot energy of 0.13 mJ was chosen for the acquisition of the temperature

Fig. 8 Temperature lifetime characteristic of $Gd_3Ga_5O_{12}$:Cr and $Gd_3Ga_5O_{12}$:Cr,Ce

luminescence in the range of 650 and 850 nm, where the upper end corresponds to the limit of the spectral range of the spectrometer. An investigation by Khalid and Kontis discussed the effect of blackbody radiation on phosphor thermometry and revealed a significant influence on temperatures above 1120 K [36]. Since the maximum temperatures measured in this work are well below 500 K, systematic influence is neglected.

Figure 8 shows a comparison of the temperature lifetime characteristic of the commercially available phosphor $Gd_3Ga_5O_{12}$:Cr and the custom-synthesized material with a Cr concentration of 2 mol% and co-doping with 0.034 mol% of Ce. Calibration data were acquired from 300 to 500 K with a laser repetition rate of 1 kHz. Each dot represents the mean value of $N = 500$ individually evaluated single-shots at a laser energy of 0.13 mJ per pulse. The custom-made material has a faster decay time across the entire temperature range, which can be traced back to the concentration of the main dopant [37], which is
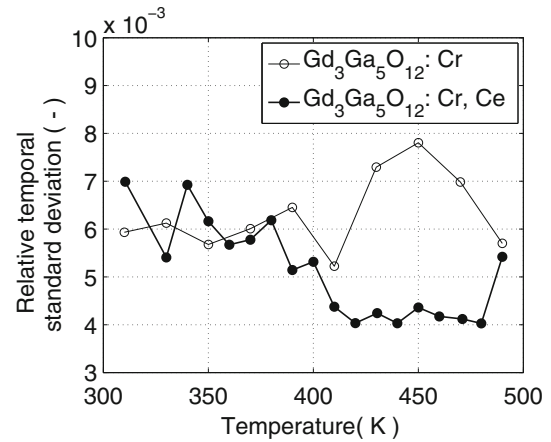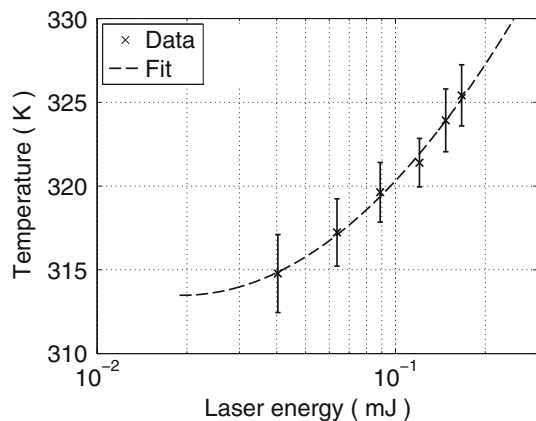
Fig. 10 Laser-induced heating of $Gd_3Ga_5O_{12}$:Cr,Ce at MP1 and engine at standstill
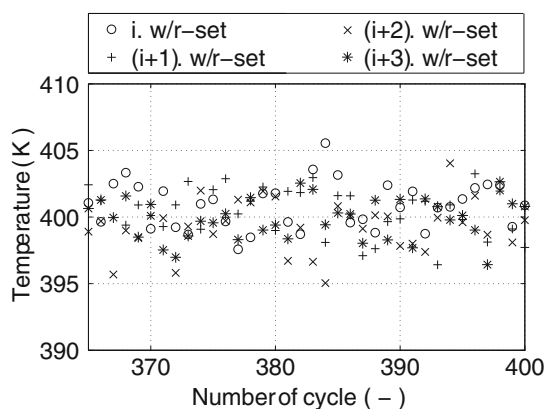

Fig. 11 Single-shot results of the standard operational point for 36 consecutive cycles of 4 consecutive work-rest sets. Data were acquired at −180 CAD

lifetime characteristic and the measurements shown in Sect. 5.

The systematic error caused by laser heating was corrected for by the calibration procedure. To measure the temperature lifetime characteristic presented in Fig. 8, the phosphor was coated on the front end of a $20 \times 10 \times 2$ mm^3 stainless steel substrate. The thermocouple to which the lifetimes were referred was fixed at the opposite side. When illuminating the phosphor coating using the pulsed UV laser, the temperature measured by the thermocouple at the opposite side was not influenced. This is due to the high thermal inertia and heat capacity of the stainless steel substrate. Because of this, phosphor lifetimes as measured for apparent temperatures (including the effect of laser heating) were related to unbiased temperatures yielding an accurate calibration for this specific laser energy density. For the scenario presented in Fig. 10, a cylinder head temperature of approximately 323 K could be determined, which is in agreement with previous measurements using identical engine settings [23].

Additionally, this result was verified by the temperature reading of a surface-mounted type K thermocouple.

5 In-cylinder measurements

As a reference for all parameter variations performed, a standard operational point was defined with $\lambda = 1.2$ and ignition at −19 CAD. In the following subsections, the standard operational point is discussed for MP1 first. The measurements at different locations are then compared, followed by discussions on variations of the spark timing and the air–fuel ratio.

5.1 Standard operational point

To ensure statistically stationary boundary conditions, the engine was operated in work-rest mode, with 400 fired cycles followed by 800 motored ones. Measurements were performed when the minimum and maximum exhaust gas temperatures of consecutive work-rest sets were stable.

With a repetition rate of 1 kHz at 1000 rpm, temperatures were measured every 6th crank angle degree. Due to the settings and the on-board memory of the oscilloscope, a maximum of 36 consecutive cycles could be acquired at once. Therefore, the last 36 of every 400 fired cycles within a work-rest set were recorded. Figure 11 shows single-shot temperatures for −180 CAD of cycles 365 to 400 for 4 consecutive work-rest sets. It is obvious that the temperature is not only constant for consecutive work-rest sets but for consecutive cycles within the sets. The mean value of all measurements shown in Fig. 11 corresponds to 400.14 K with a temporal standard deviation of 1.85 K, which is very similar to the value observed during calibration measurements, which justifies the assumption of statistically stationary boundary conditions. Hence, for the following measurements, phase-locked statistics were computed for 4 consecutive work-rest sets, resulting in a total of 144 cycles.

Figure 12 shows phase-locked mean values and standard deviations for temperature and pressure for the standard operational point. Valve timing is indicated by IO—intake opening, IC—intake closing, EO—exhaust opening, and EC—exhaust closing.

During intake stroke, a slight decrease can be observed in phase-averaged temperatures due to fresh air. Subsequently to IC, compression leads to a moderate increase in temperature. Upon ignition, a steep temperature gradient can be observed, which is caused by the flame front impinging on the cylinder head. Expansion results in a decrease in temperatures, starting at 12 CAD. Following the opening of the exhaust valves, a second increase in temperatures with a delay of approximately 26 CAD with
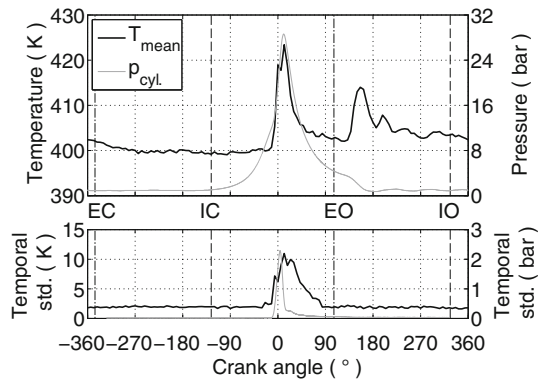
Fig. 12 Phase-averaged temperatures, in-cylinder pressures (*upper plot*), and corresponding temporal standard deviations (*lower plot*) at MP1 for the standard scenario

Fig. 13 Phase-averaged temperatures (*upper plot*) and corresponding temporal standard deviations (*lower plot*) at various measurement points for the standard operational point

respect to EO can be seen. This is caused by high Nusselt numbers at the cylinder head in between the exhaust valves. Subsequently, temperatures decrease, superimposed by an oscillation. This oscillation can also be seen with a slight phase-shift in the averaged in-cylinder pressure trace and is therefore assumed to be caused by pulsations of the exhaust gas system, as discussed in [22]. Values in the order of 2 K are observed in temporal standard deviations shown in Fig. 12, which corresponds well to the measurement precision shown in Fig. 9. Exceptions occur for −12 CAD to 90 CAD, where standard deviations of up to 11 K were measured. This can be explained by the three following reasons:

- Standard deviations of pressure, which are shown in the lower part of Fig. 12, show fluctuations of up to 9 % around top dead center (TDC). This implies cycle-to-cycle temperature fluctuations at the surface of the cylinder head.
- The correction of the time-dependent offset due to the presence of flame luminosity leads to additional uncertainty in the determination of the decay time.
- Flame luminosity is accompanied by a decrease in SNR of the phosphorescence signal of up to 80 %. This leads to additional uncertainties in the determination of τ.

The resulting measurement uncertainty is a convolution of these effects and equals in the worst case 2.6 % of the phase-averaged temperature.

5.2 Spatial variation

Figure 13 illustrates phase-averaged temperature evolutions of probe volume locations between the exhaust valves (MP1), between the intake and exhaust valves (MP2), and between the intake valves (MP3). The lower plot shows the corresponding temporal standard deviations. The overall temperature level for MP1 is highest, while the temperature
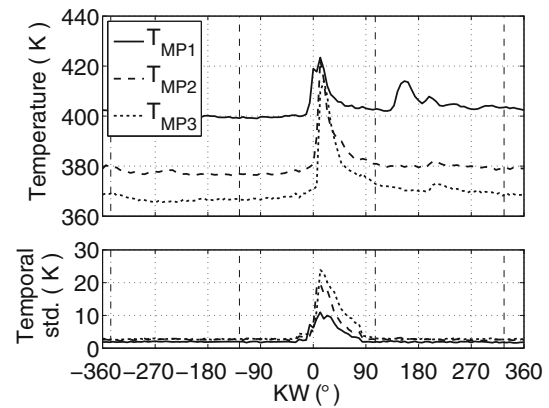
of MP2 and MP3 are about 25 and 35 K lower, respectively. Qualitatively, temperatures of different locations show similar temporal evolutions prior to ignition. The temperature gradient caused by combustion can be observed first at MP1 compared to the other measurement locations. The position and the absolute value of the maximum averaged temperature are identical for MP1–MP3. Hence, a stronger thermal cycling is evident for MP2 and MP3. During expansion and exhaust, the second maximum, which could be observed for MP1, vanishes for MP2 and MP3. A slight increase in phase-averaged temperatures is observable between 190 CAD, and 230 CAD for all measurement locations, which is shifted toward the end of the cycle with increasing distance to MP1. This supports the hypothesis that acoustic waves are responsible for these effects.

Temporal standard deviations presented in Fig. 13 are in the same order of magnitude independent of measurement locations. Around TDC, standard deviations for MP2 and MP3 are higher compared to MP1. Since cycle-to-cycle temperature fluctuations are expected to be similar for all locations, the differences in standard deviations are attributed to local differences in the flame luminescence intensities.

5.3 Variation in spark timing

To quantify the effect of spark timing on the cylinder head temperature evolution, temperatures were determined at MP1 for a spark timing of −9 CAD, −19 CAD and −29 CAD. The results for phase-locked temperatures and standard deviations are shown in Fig. 14. To aid interpretation of temperature evolutions, Fig. 15 presents phase-locked pressures and corresponding standard deviations.

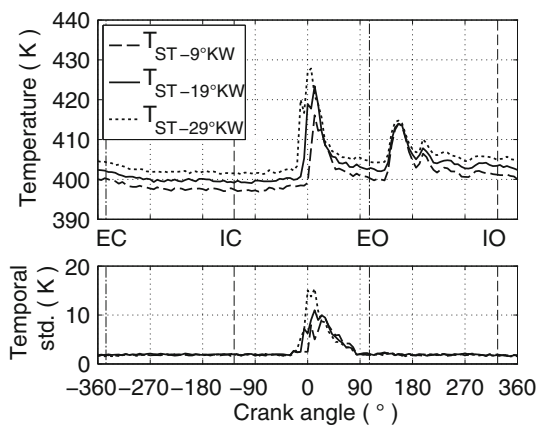In general, the following effects can be observed:

Fig. 14 Phase-averaged temperatures (*upper plot*) and corresponding temporal standard deviations (*lower plot*) at various spark timings for MP1
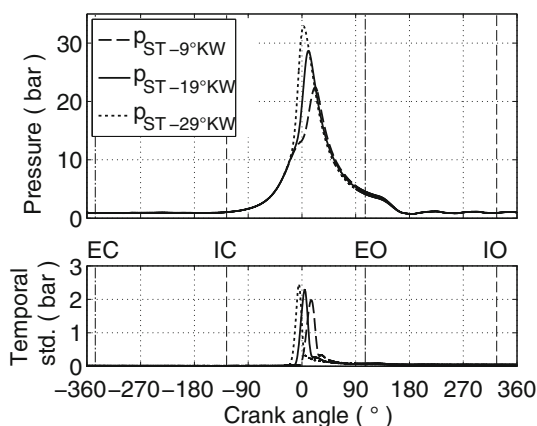

Fig. 15 Phase-averaged pressures (*upper plot*) and corresponding temporal standard deviations (*lower plot*) at various spark timings

- The later the spark timing, the lower the temperature level of the corresponding cycles. The overall difference in temperature levels during intake equals about 2 K per spark timing shift of 10 CAD.
- The instance in time of the combustion-caused temperature gradient corresponds well to the evolution of in-cylinder pressures. Hence, early spark timing leads to an early temperature gradient. This effect can also be seen in the corresponding standard deviations of temperature and pressure.
- The temperature oscillation during expansion and exhaust is independent of spark timing. Phase and amplitude of all three STs shown reveal an identical systematic, with a common local temperature maximum at 156 CAD.
- The temporal standard deviation is about 2 K except for crank angles near TDC where flame luminosity is high. This corresponds well to the precision of the calibration measurements (Sect. 4.2) and indicates stable wall temperatures within the observed cycles.

5.4 Variation in air–fuel ratio

The final experiment incorporates measurements with different air–fuel ratios investigated at MP1. To ensure stable engine conditions, parameters were adjusted according to Table 2.

Results of the temperature measurements are presented in Fig. 16 for mean values (upper plot) and temporal standard deviations (lower plot). As in the preceding

Table 2 Engine operational parameters for air–fuel ratio variations

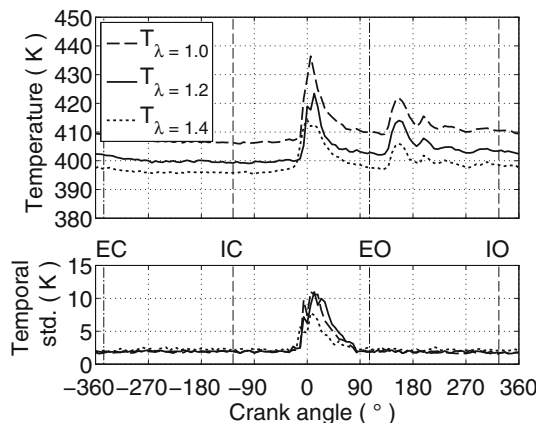| Air–fuel ratio	Spark timing	Injection period	Mean effective pressure
1.0	−19 CAD	7.65 ms	5.36 bar
1.2	−19 CAD	6.65 ms	5.11 bar
1.4	−32.5 CAD	5.65 ms	4.42 bar

Fig. 16 Phase-averaged temperatures (*upper plot)* and corresponding temporal standard deviations (*lower plot)* at various air–fuel ratios for MP1
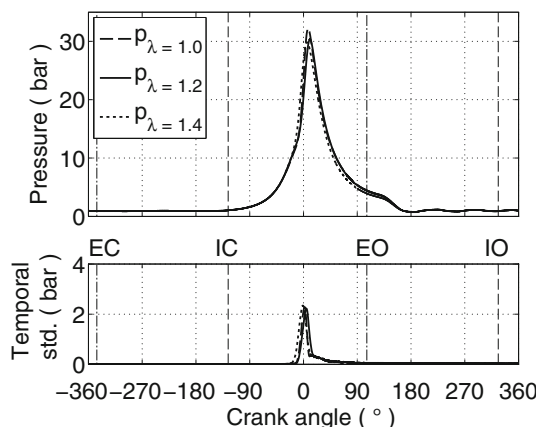

Fig. 17 Phase-averaged pressures (*upper plot*) and corresponding temporal standard deviations (*lower plot*) at various air–fuel ratios

Section, corresponding in-cylinder pressure data are shown in Fig. 17.

The highest temperature level is observed in stoichiometric conditions. The lowest level of temporal temperature standard deviations around TDC is measured at $\lambda = 1.4$. The excess of air is accompanied by lower flame luminosity and leads to more precise offset and temperature determination.

In temporal pressure standard deviations, the pressure fluctuations are identical for the engine conditions investigated, which supports the hypothesis that the variations in phase-locked temperature standard deviations are attributable to the measurement technique.

6 Summary

High-speed phosphor thermometry was applied to measure cylinder head temperatures within an optically accessible internal combustion engine under fired operation. The thermographic phosphor material $Gd_3Ga_5O_{12}$:Cr,Ce was synthesized with a special composition to satisfy the requirements of the measurement technique and the device under test. In addition to the characterization of the sensor material for precision and accuracy, measurements of temperature evolutions for different positions at the cylinder head under fired engine conditions were shown. The effects of spark timing and air–fuel ratio on cylinder head temperatures were investigated. The results of these experiments confirm the ability of high-speed phosphor thermometry to determine fast temperature gradients with a high degree of precision and accuracy. Additionally, the total time for performing the engine experiments with these statistics was orders of magnitude lower than it would have been when using conventional phosphor thermometry at repetition rates in the order of 10 Hz.

References

1. C. Rakopoulos, G. Kosmadakis, E. Pariotis, Critical evaluation of current heat transfer models used in cfd in-cylinder engine simulations and establishment of a comprehensive wall-function formulation. Appl. Energy **87**(5), 1612–1630 (2010). doi:10.1016/j.apenergy.2009.09.029

2. G. Borman, K. Nishiwaki, Internal-combustion engine heat transfer. Prog. Energy Combust. Sci. **13**(1), 1–46 (1987). doi:10.1016/0360-1285(87)90005-0

3. J.A. Gatowski, M.K. Smith, A.C. Alkidas, An experimental investigation of surface thermometry and heat flux. Exp. Thermal Fluid Sci. **2**(3), 280–292 (1989). doi:10.1016/0894-1777(89)90017-4

4. M.A. Marr, J.S. Wallace, S. Chandra, L. Pershin, J. Mostaghimi, A fast response thermocouple for internal combustion engine surface temperature measurements. Exp. Thermal Fluid Sci. **34**(2), 183–189 (2010). doi:10.1016/j.expthermflusci.2009.10.008

5. S.W. Allison, G.T. Gillies, Remote thermometry with thermographic phosphors: Instrumentation and applications. Rev. Sci. Instrum. **68**(7), 2615 (1997). doi:10.1063/1.1148174

6. M. Aldén, A. Omrane, M. Richter, G. Särner, Thermographic phosphors for thermometry: A survey of combustion applications. Prog. Energy Combust. Sci. **37**(4), 422–461 (2011). doi:10.1016/j.pecs.2010.07.001

7. J. Brübach, C. Pflitsch, A. Dreizler, B. Atakan, On surface temperature measurements with thermographic phosphors: A review. Prog. Energy Combust. Sci. **39**(1), 37–60 (2013). doi:10.1016/j.pecs.2012.06.001

8. H. Aizawa, M. Sekiguchi, T. Katsumata, S. Komuro, T. Morikawa, Fabrication of ruby phosphor sheet for the fluorescence thermometer application. Rev. Sci. Instrum. **77**(4), 044902 (2006). doi:10.1063/1.2190069

9. A.L. Heyes, S. Seefeldt, J. P. Feist, Two-colour phosphor thermometry for surface temperature measurement. Opt. Laser Technol. **38**(4-6), 257–265 (2006)

10. J. Brübach, A. Patt, A. Dreizler, Spray thermometry using thermographic phosphors, Applied Physics B **83**(4), 499–502 (2006). doi:10.1007/s00340-006-2244-8

11. D. A. Rothamer, J. Jordan, Planar imaging thermometry in gaseous flows using upconversion excitation of thermographic phosphors, Appl. Phys. B **106**(2), 435–444 (2012). doi:10.1007/s00340-011-4707-9

12. B. Noel, Borella H. M., L. Franks, B. Marshall, S. W. Allison, M. R. Cates, Proposed method for remote thermometry in turbine engines, in: AIAA Paper, Los Alamos Natl Lab and Los Alamos and NM and USA and Los Alamos Natl Lab and Los Alamos and NM and USA, 1985

13. T. Kissel, E. Baum, A. Dreizler, J. Brübach, Two-dimensional thermographic phosphor thermometry using a CMOS high speed camera system, Appl. Phys. B **96**(4):731–734 (2009). doi:10.1007/s00340-009-3626-5

14. B. Atakan, C. Eckert, C. Pflitsch, Light emitting diode excitation of Cr^3+ :Al_2O_3 as thermographic phosphor: experiments and measurement strategy, Meas. Sci. Technol. **20**(7), 075304 (2009). doi:10.1088/0957-0233/20/7/075304

15. S. W. Allison, J. R. Buczyna, R. A. Hansel, Walker D. G., G. T. Gillies, Temperature-dependent fluorescence decay lifetimes of the phosphor y_3(al_0.5ga_0.5)_5o_12:ce 1%. J. Appl. Phys. **105**(3), 036105-+ (2009). doi:10.1063/1.3077262

16. N. Fuhrmann, J. Brübach, A. Dreizler, Phosphor thermometry: A comparison of the luminescence lifetime and the intensity ratio approach. Proc. Combust. Inst. **34**(2), 3611–3618 (2013). doi:10.1016/j.proci.2012.06.084

17. J.S. Armfield, R.L. Graves, D.L. Beshears, M.R. Cates, T.V. Smith, S.W. Allison, Phosphor thermometry for internal combustion engines. SAE Technical Paper Series (971642)

18. A. Omrane, F. Ossler, M. Aldén, J. Svenson, J. Pettersson, Surface temperature of decomposing construction materials studied by laser-induced phosphorescence. Fire Mater. **29**(1), 39–51 (2005)

19. T. Husberg, S. Girja, I. Denbratt, A. Omrane, M. Aldén, J. Engström, Piston temperature measurements by use of thermographic phosphors and thermocouples in a heavy-duty diesel engine run under partly premixed conditions. SAE International 2005-01-1646

20. C. Knappe, P. Andersson, M. Algotsson, M. Richter, J. Lindén, M. Aldén, M. Tuner, B. Johansson, Laser-induced phosphorescence and the impact of phosphor coating thickness on crank-

angle resolved cylinder wall temperatures. SAE Technical Paper 2011-01-1292. doi:10.4271/2011-01-1292

21. S. Someya, M. Uchida, K. Tominaga, H. Terunuma, Y. Li, K. Okamoto, Lifetime-based phosphor thermometry of an optical engine using a high-speed cmos camera. Int. J. Heat Mass Transf. **54**(17-18), 3927–3932 (2011). doi:10.1016/j.ijheatmasstransfer.2011.04.032

22. N. Fuhrmann, M. Schild, D. Bensing, S. A. Kaiser, C. Schulz, J. Brübach, A. Dreizler, Two-dimensional cycle-resolved exhaust valve temperature measurements in an optically accessible internal combustion engine using thermographic phosphors, Appl. Phys. B **106**(4), 945–951 (2012). doi:10.1007/s00340-011-4819-2

23. N. Fuhrmann, E. Baum, J. Brübach, A. Dreizler, High-speed phosphor thermometry, Rev. Sci. Instrum.**82**(10), (2011) 104903. doi:10.1063/1.3653392

24. J. Brübach, T. Kissel, M. Frotscher, M. Euler, B. Albert, A. Dreizler, A survey of phosphors novel for thermography, J. Lumin. **131**(4), 559–564 (2011). doi:10.1016/j.jlumin.2010.10.017

25. T. Kissel, J. Brübach, F.M., C. Litterscheid, A. Albert, A. Dreizler, Phosphor thermometry: On the synthesis and characterisation of $Y_3Al_5O_{12}$:Eu (YAG:Eu) and $YAlO_3$:Eu (YAP:Eu), Materials Chemistry and Physics, accepted

26. E.L. Dukhovskaya, Y.G. Saksonov, A.G. Titova, Oxygen parameters of certain compounds with the garnet structure. Neorg. Mater. **9**, 809 (1973)

27. A.X.S. Bruker, TOPAS V2.1: General profile and structure analysis software for powder diffraction data (2003)

28. B. Atakan, D. Roskosch, B. Atakan, D. Roskosch, Thermographic phosphor thermometry in transient combustion: A theoretical study of heat transfer and accuracy. Proc. Combust. Inst. **34**(2), 3603–3610 (2013). doi:10.1016/j.proci.2012.05.022

29. M.A. Everest, D.B. Atkinson, Discrete sums for the rapid determination of exponential decay constants. Rev. Sci. Instrum. **79**(2), 023108 (2008). doi:10.1063/1.2839918

30. N. Fuhrmann, J. Brübach, A. Dreizler, On the mono-exponential fitting of decay curves., Applied Physics B: Lasers and Optics, submitted

31. J. Brübach, J. Janicka, A. Dreizler, An algorithm for the characterisation of multi-exponential decay curves, Opt. Lasers Eng. **47**(1), 75–79 (2009). doi:10.1016/j.optlaseng.2008.07.015

32. N. Fuhrmann, T. Kissel, A. Dreizler, J. Brübach, $Gd_3Ga_5O_{12}$:Cr-a phosphor for two-dimensional thermometry in internal combustion engines, Meas. Sci. Technol. **22**(4), 045301 (2011). doi:10.1088/0957-0233/22/4/045301

33. G. Blasse, B.C. Grabmaier, M. Ostertag, The afterglow mechanism of chromium-doped gadolinium gallium garnet, J. Alloys Compd. **200**(1-2), 17–18 (1993). doi:10.1016/0925-8388(93)90464-X

34. H. M. Rietveld, A profile refinement method for nuclear and magnetic structures, J. Appl. Crystallogr. **2**(2), 65–71 (1969). doi:10.1107/S0021889869006558

35. C. Greskovich, S. Duclos, Ceramic scintillators. Annu. Rev. Mater. Sci. 27(1), 69–88 (1997). doi:10.1146/annurev.matsci.27.1.69

36. A. Khalid, K. Kontis, Thermographic phosphors for high temperature measurements: Principles, current state of the art and recent applications. Sensors **8**(9), 5673–5744 (2008)

37. J. Brübach, J.P. Feist, A. Dreizler, Characterization of manganese-activated magnesium fluorogermanate with regards to thermographic phosphor thermometry, Measurement Science and Technology 19(2), 025602 (2008). doi:10.1088/0957-0233/19/2/025602